

# JGR Solid Earth



## RESEARCH ARTICLE

10.1029/2022JB025132

# Influence of Fluids on Earthquakes Based on Numerical Modeling

Valentin Marguin<sup>1</sup>  and Guy Simpson<sup>1</sup>

<sup>1</sup>Department of Earth Sciences, University of Geneva, Geneva, Switzerland

### Key Points:

- Properties of earthquakes are markedly influenced by the presence of fluid overpressures
- Ruptures in wet models have relatively low stress drops, sliding speed and rupture velocity
- Slow slip events and aftershocks might be a fingerprint of fluid overpressures

### Correspondence to:

V. Marguin,  
valentin.marguin@unige.ch

### Citation:

Marguin, V., & Simpson, G. (2023). Influence of fluids on earthquakes based on numerical modeling. *Journal of Geophysical Research: Solid Earth*, 128, e2022JB025132. <https://doi.org/10.1029/2022JB025132>

Received 12 JUL 2022

Accepted 20 JAN 2023

### Author Contributions:

**Conceptualization:** Valentin Marguin, Guy Simpson

**Formal analysis:** Valentin Marguin, Guy Simpson

**Funding acquisition:** Guy Simpson

**Investigation:** Valentin Marguin, Guy Simpson

**Supervision:** Guy Simpson

**Writing – original draft:** Valentin Marguin, Guy Simpson

**Writing – review & editing:** Valentin Marguin, Guy Simpson

© 2023. The Authors.

This is an open access article under the terms of the [Creative Commons Attribution License](https://creativecommons.org/licenses/by/4.0/), which permits use, distribution and reproduction in any medium, provided the original work is properly cited.

**Abstract** The strength and sliding behavior of faults in the crust is largely controlled by friction and effective stress, which is itself modulated by fluid pressure. Most earthquake models assume a fixed pore fluid pressure despite widespread evidence that it varies strongly in time due to changes in permeability. Here we explore how dynamic changes in pore pressure influence the properties of earthquakes in the upper crust. To study this problem we develop a two dimensional model that incorporates slow tectonic loading and fluid pressure generation during the interseismic period with frictional sliding on a thrust fault whose permeability evolves with slip. We find that the presence of relatively modest fluid overpressures tends to reduce coseismic slip, stress drop, maximum sliding velocity, rupture velocity and the earthquake recurrence time compared to models without fluids. Our model produces a wide range of sliding velocities from rapid to slow earthquakes, which occur due to the presence of high pore pressures prior to rupture. The models also show evidence for aftershocks that are driven by fluid transfer along the fault plane after the mainshock. Overall, this study shows that fluids can exert an important influence on earthquakes in the crust, which is mostly due to modulation of the effective stress and variations in permeability, and to a lesser extent to poro-elastic coupling.

**Plain Language Summary** In this study we use a numerical model to investigate how fluid pressures vary over the seismic cycle and how they interact with and influence the properties of earthquakes that occur in the upper crust. In the model, fluid overpressures are generated slowly during the interseismic period by phenomena such as dehydration reactions while they are episodically released during earthquakes due to fracturing and a dramatic increase in permeability. The models show that the presence of high fluid pressures has an important influence on earthquakes. High fluid pressures favor smaller, more frequent earthquakes. Also high fluid pressures may sometimes be responsible for aftershocks and for anomalously slow earthquakes that involve slip over several months rather than several seconds. Overall, we show that the presence of fluids in the crust plays an integral part in the earthquake process.

## 1. Introduction

Understanding the physical parameters that modulate seismicity and that control the properties of earthquakes remains an ongoing challenge in earthquake mechanics. Several factors play a key role, one of which is the fault strength, which in the upper crust is determined by the product of the friction coefficient and the effective normal stress (i.e., the total normal stress minus fluid pressure). Much attention has been focused on how fault strength varies due to changes in the friction coefficient (Dieterich, 1978; Marone, 1998; Ruina, 1983; Scholz, 1998). These experimental studies have resulted in a detailed constitutive law that is now commonly referred to as rate-and-state friction. Changes in friction are quite subtle at relatively low sliding velocities (i.e., <1 mm/s) (Dieterich, 1978; Ruina, 1983), but they may become profound at slip rates similar to those typically encountered during fast earthquakes where thermal weakening and other mechanisms can be activated (Di Toro et al., 2004; Goldsby & Tullis, 2011; Noda et al., 2009; Rice, 2006; Tsutsumi & Shimamoto, 1997). These results provide a basis for understanding why some faults can slip at anomalously low shear stress (Scholz, 2006). However, most earthquake stress drops are between 1 and 10 MPa (Abercrombie & Rice, 2005; Allmann & Shearer, 2009), which suggests that shear stress levels must also be low prior to rupture (Noda et al., 2009, 2011). If this was not the case, the combination of dramatic coseismic weakening and high ambient shear stress would lead to much larger stress drops than observed. One way this might be achieved is with elevated pore pressures, which would reduce the effective normal stress, and thus enable earthquakes to initiate at relatively low shear stress (Liu et al., 2005; Rice, 2006; Simpson, 2018).

There are a number of mechanisms that could act to increase fluid pressures during the interseismic period at depths where earthquakes are typically nucleated (~10 km) (Osborne & Swarbrick, 1998). For example, fluids are being continuously released from dehydration reactions (Connolly, 1997; Leclère et al., 2018) and cooling magmas at these and greater depths (Hedenquist & Lowenstern, 1994; Weis et al., 2012), which owing to their low density, rise toward the surface. Concomitantly with this, compaction (viscous or elastic) closes pores and cracks and reduces permeability, thereby hindering the escape of fluids and increasing the fluid pressure (Walder & Nur, 1984). Numerous studies have provided evidence to suggest that fluid pressures in the crust are elevated, sometimes approaching the lithostatic pressure (Etheridge et al., 1984; Fisher et al., 1995; Sibson, 2017; Suppe, 2014).

The long term build up of fluid overpressure in the upper crust is counteracted by more rapid processes related to the onset of brittle fracture and/or frictional sliding on preexisting faults due to dilatancy and permeability enhancement that enable excess pore pressures to dissipate (Miller & Nur, 2000; Segall & Rice, 1995; Sibson, 1990). Substantial evidence shows that faults transiently act as major fluid conduits and that this is associated with rapid and dramatic drops in fluid pressure (Cox, 2005; Sibson et al., 1988). Fault rocks are typically highly fractured and cemented, which suggests that the permeability repeatedly cycles between high and low values (Chester & Logan, 1986; Cox & Munroe, 2016). Collectively, these observations have led to the notion that some major faults act as pressure valves, sporadically slipping and releasing fluid overpressures before resealing and enabling shear stresses and fluid overpressures to be reestablished (Cox, 2005; Sibson, 1990, 1992). This is commonly known as fault valve behavior (Sibson, 1990).

Despite the wealth of field evidence supporting the concept of fault-valve behavior, it is noteworthy that most earthquake models do not explicitly account for variations in fluid pressure with sliding. Many models assume a highly overpressured fault, a requirement that is necessary in order to obtain realistic stress drops and slip behavior (Lapusta et al., 2000; Lapusta & Rice, 2003; Liu et al., 2005). However, if permeabilities on a fault increase dramatically during sliding as evidence suggests (Cox, 2005; Sibson et al., 1988), then the fluid pressure is likely to change rapidly during an earthquake, which could potentially impact on rupture dynamics. Various workers have studied different aspects of fault-valve behavior using modeling and have shown that fluids might be responsible for aftershocks, transient creep, seismic swarms, and in general, smaller seismic events (Dal Zilio & Gerya, 2022; Dal Zilio et al., 2022; Miller et al., 2004; Petrini et al., 2020; Sleep & Blanpied, 1992; Zhu et al., 2020). However, of these studies, only Dal Zilio et al. (2022) considers both variations in fluid pressure and full poroelastic coupling.

In this work, we focus on how earthquakes are modulated by long-term generation of fluid overpressures during the interseismic period coupled with rapid changes in fluid pressure caused by a sharp increase in the fault permeability during rupture. This is achieved by studying a two dimensional mechanical model based on sliding on a thrust fault governed by rate- and state-dependent friction (Dieterich, 1978; Ruina, 1983) coupled to poro-viscoelastic deformation and fluid flow in the surrounding crust. Our model shares some similarities with the study of Zhu et al. (2020) except that we incorporate full poro-elasticity, 2D fluid flow (i.e., on and off-fault), and more dramatic coseismic variations in permeability. Although the model presented is generic and not applied to any specific case, the setup and parameters are chosen to be representative of a continental convergent plate boundary setting.

## 2. Governing Equations

We simulate ruptures on a preexisting 30° dipping reverse fault embedded within a 15 km thick poro-elastic layer that overlies a 15 km thick poro-viscoelastic substrate (see Figure 1a). The entire domain is pushed laterally over a rigid base at 25 mm/year. The upper boundary is a free surface. Model parameters are summarized in Table 1.

Deformation of the porous solid is governed by combining force balance with the constitutive relations for a viscoelastic material. Assuming quasi-static conditions, the two dimensional force balance equation can be written as

$$B^T(\sigma' - \alpha m P_f) = -[0, -\rho g]^T \quad (1)$$

where  $\sigma'$  is the effective stress vector (using Voigt notation),  $\alpha$  is Biot's coefficient,  $m$  is the vector form of Kronecker's delta ( $\delta_{ij}$ ),  $P_f$  is the fluid pressure,  $\rho$  is the rock density, and  $g$  is the acceleration due to gravity. The differential operator  $B$  is defined as

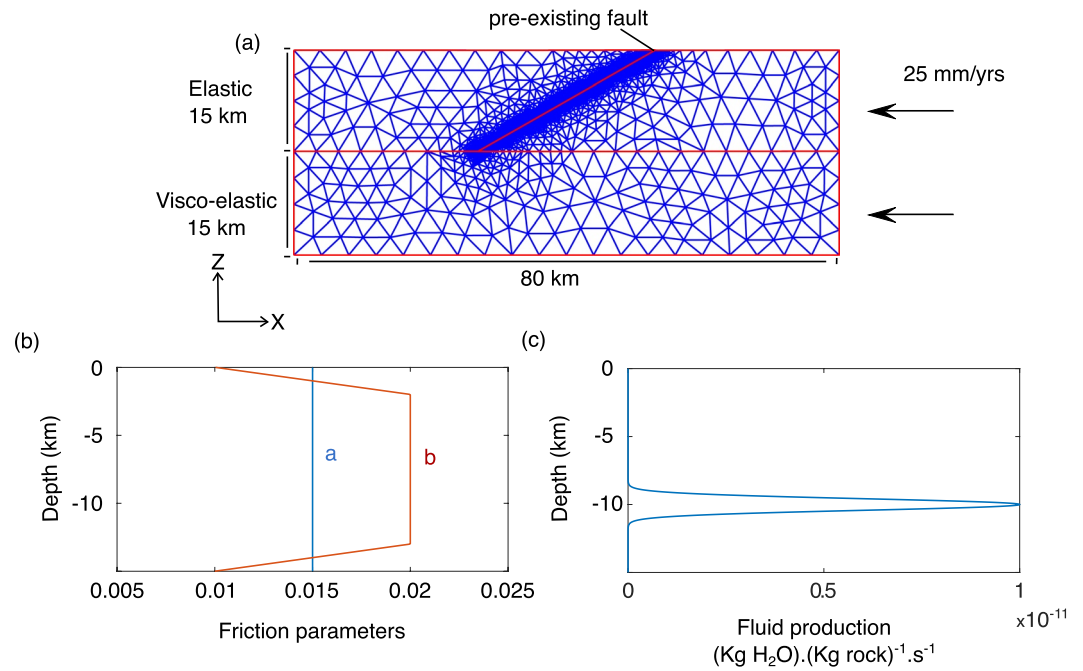


**Figure 1.** (a). Typical FEM model setup for 2D simulation (Simpson, 2018), (b). Rate and state friction parameters in the upper elastic layer (see Equation 8), (c). Fluid production rate in model with  $S_0 = 10^{-11}$  (kg H<sub>2</sub>O) (kg rock)<sup>-1</sup> s<sup>-1</sup> (see Equations 6 and 13).

$$B = \begin{bmatrix} \frac{\partial}{\partial x} & 0 \\ 0 & \frac{\partial}{\partial z} \\ \frac{\partial}{\partial z} & \frac{\partial}{\partial x} \end{bmatrix} \quad (2)$$

The stress–strain relation for an isotropic Maxwell viscoelastic material can be written as

$$\frac{\partial \sigma'}{\partial t} = D \frac{\partial \epsilon}{\partial t} + D_0 \sigma' \quad (3)$$

where  $D$  and  $D_0$  are viscoelastic material matrices and  $\epsilon$  is the strain vector. The kinematic relation between strains and velocities (assuming small strains) can be written as

$$\frac{\partial \epsilon}{\partial t} = BV \quad (4)$$

where  $V$  the velocity vector. Combining the last two equations (i.e., Equations 3 and 4), gives

$$\frac{\partial \sigma'}{\partial t} = DBV + D_0 \sigma' \quad (5)$$

We discretize this equation using a forward Euler finite difference approximation and substitute it into 1 to leave a system of equations with velocities and fluid pressure as the unknowns.

The equation governing fluid pressure is obtained by combining mass balance of the fluid with Darcy's law. This equation can be written as

$$\beta \frac{\partial P_e}{\partial t} = \nabla \cdot \left( \frac{k}{\eta_f} \nabla P_e \right) - \alpha m^T BV + S \quad (6)$$

where  $P_e$  the fluid pressure in excess of hydrostatic (i.e.,  $P_e = P_f - \rho_f g z$ ),  $\beta$  is the effective bulk compressibility (which subsumes the porosity, fluid compressibility, solid compressibility, etc),  $\nabla$  is the gradient operator,  $k$  the

**Table 1**  
*Model Parameters*

Parameter	Symbol	Value
Domain dimension	$D_z, D_x$	30 km, 80 km
Fault dip		30°
Boundary velocity	$V_B$	25 mm/yr
Shear modulus	$\mu$	30 GPa
Shear wave speed	$C_s$	3 km/s
Viscosity of upper layer	$\eta_{UC}$	10 <sup>32</sup> Pa.s
Viscosity of lower layer	$\eta_{LC}$	10 <sup>19</sup> Pa.s
Gravity	$g$	9.81 m/s <sup>2</sup>
Rock density	$\rho$	2700 kg/m <sup>3</sup>
Fluid density	$\rho_f$	1000 kg/m <sup>3</sup>
Biot's coefficient	$\alpha$	1
Fluid viscosity	$\eta_f$	1.83.10 <sup>-4</sup> Pa.s
Effective bulk compressibility	$\beta$	5.10 <sup>-10</sup> Pa <sup>-1</sup>
Fluid source parameter	$Z_0$	10 km
Fluid source parameter	$H$	1000 m
Fluid source parameter	$S_0$	10 <sup>-10</sup> –10 <sup>-13</sup> (kg H <sub>2</sub> O)/(kg rock) <sup>-1</sup> s <sup>-1</sup>
Permeability parameter	$\sigma^*$	30 MPa
Healing time scale	$T_H$	2 years
Sliding time scale	$T_S$	1 s
Maximum fault permeability	$k_{max}$	10 <sup>-8</sup> –10 <sup>-9</sup> m <sup>2</sup>
Minimum rock permeability	$k_{min}$	10 <sup>-19</sup> m <sup>2</sup>
Permeability parameter	$k_0$	10 <sup>-12</sup> m <sup>2</sup>
Critical sliding velocity	$V_c$	10 <sup>-3</sup> m/s
Direct effect parameter	$a$	0.015
State evolution parameter	$b$	see Figure 1b
State evolution distance	$d_c$	0.025 m
Reference velocity	$V_0$	10 <sup>-6</sup> m/s
Reference friction coefficient	$f_0$	0.6
Radiation damping term	$\Omega$	5 MPa.s/m

permeability (considered to vary as a function of sliding rate and effective stress, as outlined below),  $\eta_f$  is the viscosity of the fluid,  $\alpha$  is Biot's coefficient,  $V$  are velocities of the solid, and  $S$  is a fluid pressure source term (with units (kg H<sub>2</sub>O)/(kg rock)/s) that varies of a function of space (see below). This equation states that variations in fluid pressures occur in response to three effects: porous flow (term 1 on the right hand side of Equation 6), volumetric deformation of the poro-viscoelastic solid (term 2) and fluid production (term 3).

Fault motion is governed by Coulomb behavior combined with rate- and state-dependent friction. Here, the Coulomb condition is modified to account for radiation damping

$$\tau = f(V_f, \theta)\sigma'_n + \Omega V_f \quad (7)$$

where  $\tau$  is the shear stress,  $\sigma'_n$  is the effective normal stress,  $\Omega$  is the radiation damping term (where  $\Omega = \mu/2c_s$ , with  $\mu$  being the shear modulus and  $c_s$  the shear wave speed), and  $f(V_f, \theta)$  is the friction coefficient that is given by (Dieterich, 1979; Marone, 1998; Ruina, 1983)

$$f(V_f, \theta) = f_0 + a \ln\left(\frac{V_f}{V_0}\right) + b \ln\left(\frac{\theta}{\theta_0}\right) \quad (8)$$

In this equation,  $f_0$  is the friction coefficient at a reference sliding rate  $V_0$ ,  $V_f$  is the sliding velocity,  $a$  is a dimensionless friction parameter measuring the strength of the direct velocity dependency,  $b$  is a dimensionless coefficient measuring the strength of the state dependence (see Figure 1b),  $\theta$  is a state variable (that can be interpreted as the average age of an asperity on the fault), and  $\theta_0$  is the state variable at  $V_0$ . In this work, we use the aging law for evolution of the state (Dieterich, 1979):

$$\frac{\partial \theta}{\partial t} = 1 - \frac{V_f \theta}{d_c} \quad (9)$$

where  $d_c$  is the state evolution distance. Our approach to solve for the sliding rate on the fault is as follows: (a) solve the equations governing deformation of the poro-viscoelastic solid for the shear stress on the fault (see Equation 5), (b) set the result to the Coulomb condition (see Equation 7 combined with Equation 8), and (c) solve for the fault slip rate  $V_f$ .

The permeability is an important but poorly constrained variable, varying by at least 10 orders of magnitude under upper crustal conditions (Manning & Ingebritsen, 1999). Experiments have shown that permeability depends strongly on the effective confining pressure due to elastic closure of cracks and pores (Brace et al., 1968; Evans et al., 1997; Rice, 1992). Here, we assume that this can be described by the relation (Rice, 1992)

$$k_p = k_{\min} + (k_0 - k_{\min}) \exp\left(\frac{\bar{\sigma}'}{\sigma^*}\right) \quad (10)$$

where  $k_p$  is the pressure-dependent permeability,  $k_0$  is the permeability when the mean effective stress is null,  $k_{\min}$  is the minimum background permeability,  $\bar{\sigma}'$  is the mean effective stress (negative in compression), and  $\sigma^*$  is a parameter measuring the sensitivity of permeability to the effective confining pressure. Experiments show that  $\sigma^*$  is equal to  $\sim 30$  MPa [typically of the order of 10 MPa (Brace et al., 1968; Evans et al., 1997)]. The fault permeability is also known to change drastically over the duration of the seismic cycle (Miller, 1997). Rapid sliding during an earthquake can produce an extremely high permeability due to fracturing and dilatancy (Cox & Munroe, 2016; Heap & Kennedy, 2016; Im et al., 2019; Ishibashi et al., 2018; Lamur et al., 2017; Sibson, 1986) whereas after an earthquake compaction and mineral precipitation act to reduce permeability (Renard et al., 2000; Tenthorey et al., 2003). We capture these mechanisms using the following heuristic evolution equations

$$\begin{aligned} \frac{\partial k_f}{\partial t} &= \frac{k_{\max} - k_f}{T_S} & \text{if } V_f \geq V_c \\ \frac{\partial k_f}{\partial t} &= \frac{k_{\min} - k_f}{T_H} & \text{if } V_f < V_c \end{aligned} \quad (11)$$

where  $k_f$  is the permeability on the fault,  $k_{\max}$  corresponds to the maximum fault permeability during an earthquake,  $k_{\min}$  is the minimum permeability,  $V_f$  is the fault slip rate,  $V_c$  is a critical sliding velocity, and  $T_S$  and  $T_H$  are characteristic time scales for the permeability to increase (due to sliding during an earthquake) and decrease (by healing), respectively. The first equation accounts for an increase in permeability once the slip rate exceeds  $V_c$ , while the second equation describes the exponential decay of permeability once rapid sliding has terminated (see Figure 2). The parameters appearing in these equations are poorly constrained owing to the complexity of the governing processes and the difficulty of obtaining measurements at the relevant spatial and temporal scales. The maximum permeability could be very high, similar to that of a highly porous sediment such as a gravel if the fault rocks become highly fractured and porous. One estimate based on very rapid fluid flow induced during an earthquake suggests a coseismic permeability on the order of  $10^{-8}$  m<sup>2</sup>, consistent with fracture apertures of between 1 and 30 mm (Noir et al., 1997). This value is high, but consistent with high permeabilities measured in experiments on fractured rocks (Heap & Kennedy, 2016; Ishibashi et al., 2018; Lamur et al., 2017). In our simulations, we investigate a range of values extending from  $10^{-8}$  to  $10^{-9}$  m<sup>2</sup>. The minimum permeability could be very low, similar to a granite or low porosity limestone. Here, we assume that  $k_{\min} = 10^{-19}$  m<sup>2</sup> (Selvadurai et al., 2005). For the evolution time scales, we take 1 s for  $T_S$  and 2 years for  $T_H$ . This latter value is within the range suggested by healing observed on natural faults (Xue et al., 2013). For injection-induced seismicity, the slip is considered seismic if the slip velocity is between 0.1 mm/s and 0.1 m/s (Gischig, 2015; McClure, 2015; McClure & Horne, 2011). Therefore, we take 1 mm/s for the critical sliding velocity ( $V_c$ ) that controls the transition between a permeability increase and decrease. The total permeability is computed as

$$k = k_p + k_f. \quad (12)$$

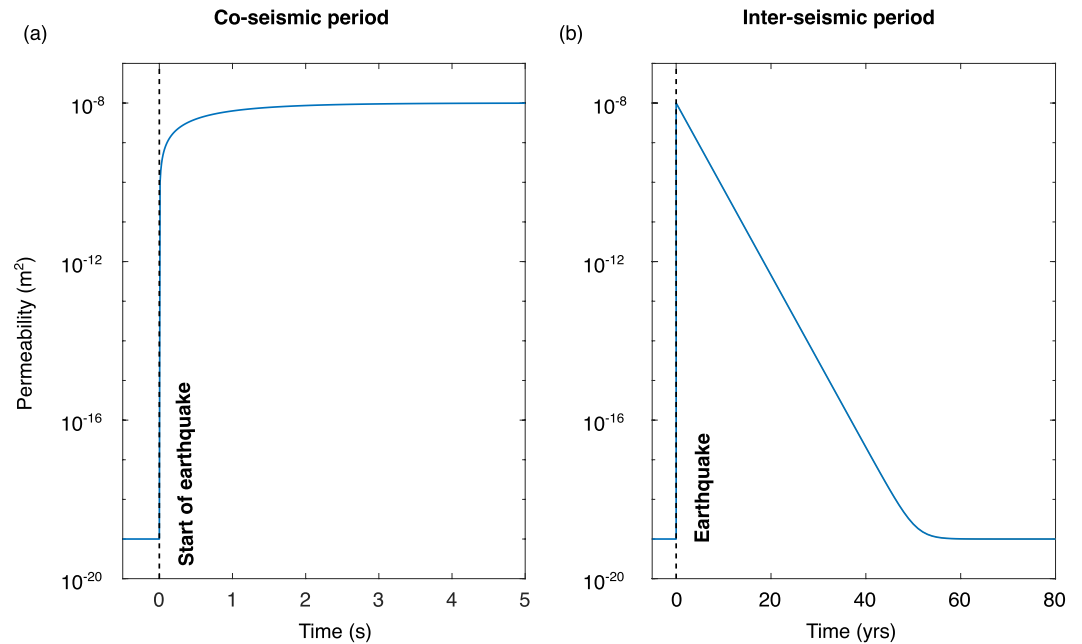


**Figure 2.** Illustration of permeability evolution (see Equation 11) on the fault during (a) co-seismic period (when  $V_f > V_c$ ) and (b) postseismic-interseismic period (when  $V_f < V_c$ ). In this example,  $k_{\min} = 10^{-19} \text{ m}^2$ ,  $k_{\max} = 10^{-8} \text{ m}^2$ ,  $T_s = 1 \text{ s}$  and  $T_H = 2 \text{ years}$ . The actually permeability variation during a model rupture can be significantly more complicated.

Note that while we incorporate permeability variations, we do not explicitly consider dilatancy (Segall & Rice, 1995).

Fluid overpressures are introduced into the model by considering a horizontal fluid source within the upper seismogenic layer (see Equation 6), which is crudely intended to mimic fluid release from a dehydration reaction. The devolatilization rate for a metamorphic dehydration reaction depends on a variety of factors including the Gibbs energy (involving temperature and pressure), the stoichiometry of the specific reaction and the surface area of the rate limiting mineral (Connolly, 1997). Here, we avoid these complexities and use a simple parametrization assuming a Gaussian function (see Figure 1c)

$$S = S_0 \exp\left(\frac{-(z - z_0)^2}{2\gamma^2}\right) \quad (13)$$

where  $z$  the depth,  $z_0$  the depth where the production rate is the greatest,  $S_0$  the maximum fluid production rate ( $(\text{kg H}_2\text{O})/(\text{kg rock})/\text{s}$ ), and  $\gamma$  is a length scale controlling the full width at half maximum ( $H$ ) of the band ( $H \approx 2.355\gamma$ ). In our simulations the fluid production layer is centered at 10 km depth and is approximately 2 km across (from top to bottom).

The above system of partial differential equations is solved for velocities and fluid pressure using the continuous Galerkin Finite Element method employing seven-node triangles and seven integration points (Simpson, 2017). We use an unstructured mesh that permits local refinement adjacent to the fault, where the nodes spacing is  $\sim 75 \text{ m}$ . This grid spacing is sufficient to resolve both the nucleation length (i.e., about 3.5 km) and the cohesion length scale (i.e., about 0.6 km), based on relations presented in Andrews (1976), and Day, et al. (2005). Our cohesive zone size is at least nine nodes, greater than the minimum size required to resolve dynamic rupture (Palmer & Rice, 1973). Adaptive time stepping is used to transition between the interseismic period (where time steps are on the order of 1 year) and times when rupture is taking place (where time steps are on the order of  $1 \mu\text{s}$ ). To obtain it, we divide an assumed maximum permitted amount of slip during a time step by the maximum calculated fault velocity.

We have performed a total of 20 simulations both with and without fluids. This study is mainly based on seven different simulations, using a range of source magnitudes and maximum fault permeabilities (see Table 1). We also performed one simulation where poroelastic coupling was neglected, which is discussed after the results

section. Most simulations presented were performed with an initial stress defined as  $\sigma_1 = 3 \sigma_3$  where  $\sigma_3$  was assumed to be given by the lithostatic (vertical) load. However, we also ran simulations with initial stresses of  $\sigma_1 = \sigma_3$  and  $\sigma_1 = 1.5 \sigma_3$ .

### 3. Results

Two main classes of simulations have been performed. A “dry” simulation was performed by setting the fluid pressure source to zero (i.e.,  $S = 0$  in Equation 6) and by constraining the permeability to a uniformly high value ( $k = 10^{-8} \text{ m}^2$ ) to avoid any fluid overpressure. Thus, the fluid pressure in the “dry” model remains hydrostatic throughout the simulation. This is compared to “wet” simulations that include fluid production and lower background permeabilities, together which lead to the generation of fluid overpressures. We omit the first two ruptures of each sequence to avoid transient effects introduced from our choice of initial conditions.

Results for a “dry” and “wet” simulation are compared in Figure 3. For the “dry” case, one sees a series of large earthquakes (red curves) that nucleate close to the base of the elastic layer and that rupture into the overlying poro-elastic medium (see Figure 3a). These are separated by periods when slip is dominated by slow creep (blue curves) at the base of the fault and close to the surface. The “wet” simulation shows a similar rupture sequence (see Figure 3b) but it differs from the results of the “dry” model in several respects. First, in the “wet” model coseismic slip is smaller and the recurrence time is shorter (both by about 50%) compared to the “dry” model (see Figure 3c). Second, in the “dry” model, the ruptures grow as expanding cracks whereas in the “wet” model they are more pulse-like (see Figures 3a and 3b). Note that in both “dry” and “wet” models, the ruptures are observed to accelerate as the upper free surface is approached. This is a feature that is special to ruptures on dip-slip faults (Oglesby et al., 1998; Scala et al., 2019). We also note that while the fluid pressure on the fault close to the fluid production zone drops during the rupture (due to the permeability increase), the fluid pressure may increase on other parts of the fault during an earthquake due to coseismic fluid transfer from more highly pressured regions. This point is discussed and illustrated more below.

The differences in the rupture sequences between “dry” and “wet” models are directly related to the control of fluid pressures on the effective normal stress and therefore to the shear stress on the fault at rupture. In the “dry” models, the shear stress is relatively elevated ( $\bar{\tau}$  approximately 100 MPa) because the fluid pressure is relatively low (see Figures 3d and 3e). In the “wet” simulation, the pore pressure ratio ( $\lambda = P_f/\sigma_z$ ) at the maximal fluid production depth (i.e., 10 km depth) oscillates between 0.37 (corresponding to a hydrostatic fluid pressure) immediately after an earthquake and  $\sim 0.5$  just prior to rupture (corresponding to a fluid overpressure of approximately 35 MPa), which enables the fault to slide at lower shear stress ( $\bar{\tau}$  approximately 90 MPa). Our observation of an important control exerted by the mean normal stress on rupture properties is consistent with observations made in many other studies (Dal Zilio & Gerya, 2022; Dal Zilio et al., 2022; Passelègue et al., 2016, 2020; Simpson, 2018; Zheng & Rice, 1998).

Because we don't have constraints on the magnitude of the fluid source term ( $S$  in Equation 6), we have performed simulations with a range of values spanning several orders of magnitude. We do not present any results with  $S_0 > 10^{-10} \text{ s}^{-1}$  (see Equation 13) because this leads to implausible surface uplift rates due to poroelastic inflation. Results show that the average peak sliding velocity, rupture speed, shear stress drop, and recurrence time all decrease systematically with the magnitude of fluid overpressure at the onset of rupture (see Figures 3 and 4). In addition, we observe that both the peak sliding velocity and the stress drop increase with increasing rupture velocity, as observed in other studies (Bizzarri, 2012; Passelègue et al., 2020). In all cases, we observed rupture velocities well below the shear wave speed.

In simulations with relatively high rates of interseismic fluid production ( $S_0 = 10^{-10} \text{ s}^{-1}$ ), we observe a series of slow slip events (SSE's) in the intervals between normal 'fast' earthquakes (see Figure 5). The slow slip events in our simulations have peak sliding velocities of  $\sim 10^{-7} \text{ m/s}$ , rupture durations of  $\sim 1$  year (see Figure 6), and stress drop of less than 1 MPa (see Figure 7).

These events have a spatial extent of about 4–5 km on the fault (see Figure 5) and they produce horizontal displacements at the surface directly above the rupture zone of about 3 cm (see Figure 6). Slow slip events are not observed when fluid production rates are lower than  $S_0 < 10^{-11} \text{ s}^{-1}$ . In this case, interseismic creep occurs only on the lower, frictionally stable portion of the fault ( $\leq 12$  km depth). For higher fluid production rates, creep can extend to lower depths where it becomes increasingly rapid because it encounters progressively higher fluid

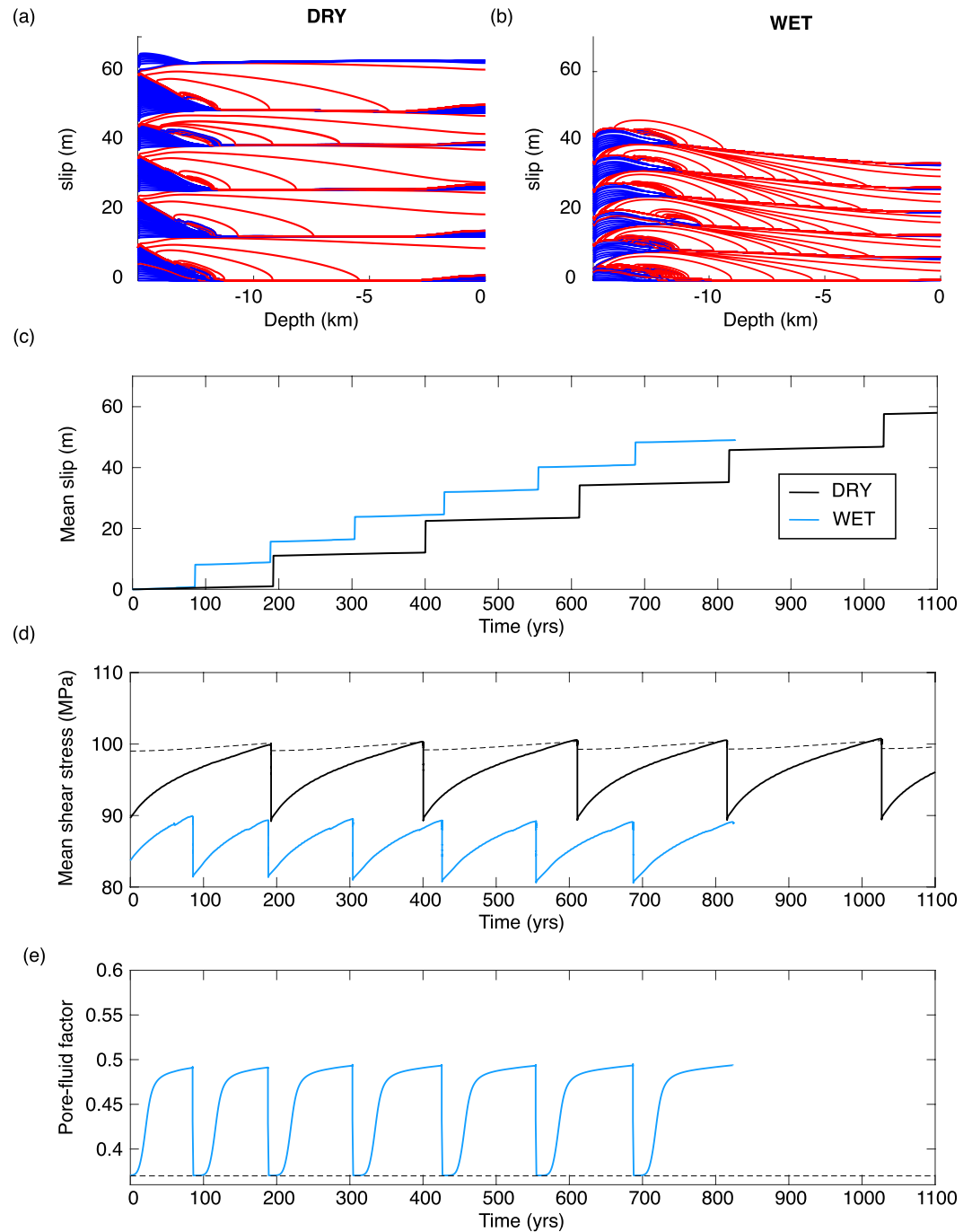


**Figure 3.** Computed rupture sequence on a reverse fault for “dry” (a) and “wet” (b) models ( $S_0 = 10^{-11} \text{ s}^{-1}$  and  $K_{\text{max}} = 10^{-8} \text{ m}^2$ ). Slip contours are plotted every 5 s during the coseismic period (red) and every 5 years during the interseismic period (blue). (c) Mean slip (m) as a function of time (years) for 2 simulations: “dry” (black curve), “wet” with fluid source (blue curve). (d) Mean shear stress  $\bar{\tau}$  versus time for the “dry” model (black curve) and the “wet” model (blue curve). The black dashed line shows the frictional strength assuming constant friction (0.6) and a hydrostatic fluid pressure. (e) Pore-fluid factor  $\lambda$  for “wet” model versus time (blue curve), at the maximum fluid production depth (i.e., 10 km depth). Black dotted line shows the pore fluid factor for a hydrostatic fluid pressure.

pressures linked to the fluid source at 10 km. These events eventually arrest as they pass through the source zone (i.e., to shallower depths) where fluid overpressures are lower. We note that the pore pressure ratio at the onset of the SSE’s in Figure 5b is approximately 0.6, indicating fluid pressures well below the lithostatic pressure.

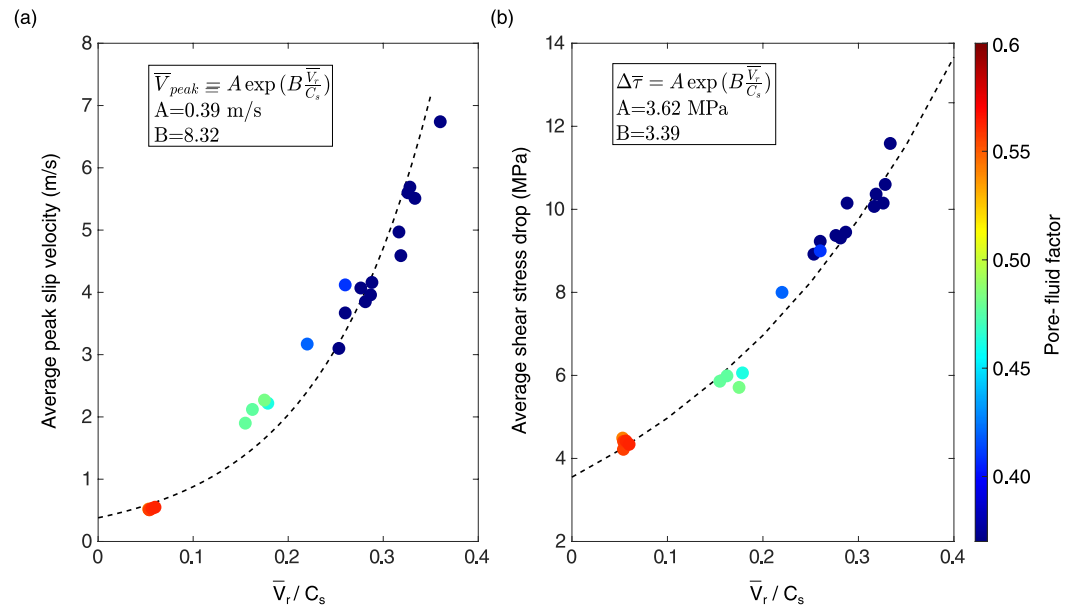


**Figure 4.** (a). Average peak sliding velocity ( $\bar{V}_{peak}$ ) as a function of the ratio between the average rupture velocity ( $\bar{V}_r$ ) and the shear wave speed ( $C_s$ ). (b) Average shear stress drop ( $\Delta\bar{\tau}$ ) as a function of the average rupture velocity over the shear wave velocity. Colorbar represents the pore-fluid factor  $\lambda$  (at the onset of fault slip), defined as the ratio of the fluid pressure to the vertical stress. We have taken the mean rupture velocity in the middle of the fault to reduce influence of the upper (free) surface.

Figure 7 shows a comparison between the slow slip events observed in “wet” models and the normal fast earthquakes observed in both “wet” and “dry” models. We observe that the SSE’s have comparable (if slightly lower) moment release but significantly longer durations (i.e., months compared to seconds) than their faster counterparts. Our observations are consistent with studies of natural earthquakes indicating that slow and fast earthquake have distinctly different scaling properties (Ide et al., 2007).

Another interesting feature that we observe in simulations with relatively high rates of interseismic fluid production ( $S_0 > 10^{-11} \text{ s}^{-1}$ ) are delayed-slip events, which we also loosely refer to as aftershocks. Note however, that we only observe isolated delayed-slip events, not multiple events that decay with time, as is typical for true aftershocks (Ōmori, 1894; Utsu, 1961; Dieterich, 1994; Scholz, 1998). One such secondary event is illustrated in Figures 8b and 8c. In this example, a large earthquake is observed to nucleate at approximately 11 km depth that propagates simultaneously downwards to the base of the fault and upward to the surface. Approximately 30 s after the nucleation of the large earthquake, a small secondary rupture occurs, which propagates downward with a sliding velocity of about 1 m/s (see Figure 8c). Rapid sliding on the fault ceases about 50 s after the nucleation of the main earthquake. However, about 16 min (960 s) after the mainshock, another rupture begins on the upper 5 km of the fault. This rupture has a peak slip rate approaching 0.1 m/s, a rupture velocity of 0.1 km/s, and a stress drop of 0.3 MPa (see Figures 7 and 8).

The delayed slip behavior is directly linked to the coseismic permeability increase on the fault during the mainshock that allows a fluid pressure pulse to rapidly migrate up and down the fault (see Figure 8d), which drives slip on previously ruptured portions of the fault. The time delay  $T_D$  between mainshock and aftershock can be estimated (from the diffusion time scale and Equation 6) roughly as

$$T_D \approx \frac{L^2 \eta_f \beta}{k_{\max}} \quad (14)$$

where  $k_{\max}$  is the coseismic permeability,  $L$  the fluid “diffusion” distance (along the fault),  $\eta_f$  is the fluid viscosity and  $\beta$  is the effective compressibility. For the simulation in Figure 8b,  $T_D$  is estimated to be approximately 1,000 s (assuming  $L = 10 \text{ km}$ ,  $\eta_f = 1.83 \times 10^{-4} \text{ Pa}\cdot\text{s}$ ,  $\beta = 5 \times 10^{-11} \text{ Pa}^{-1}$  and  $k_{\max} = 10^{-9} \text{ m}^2$ ), which is of the same order as the observed time between the mainshock and the “aftershock” (see Figure 9).

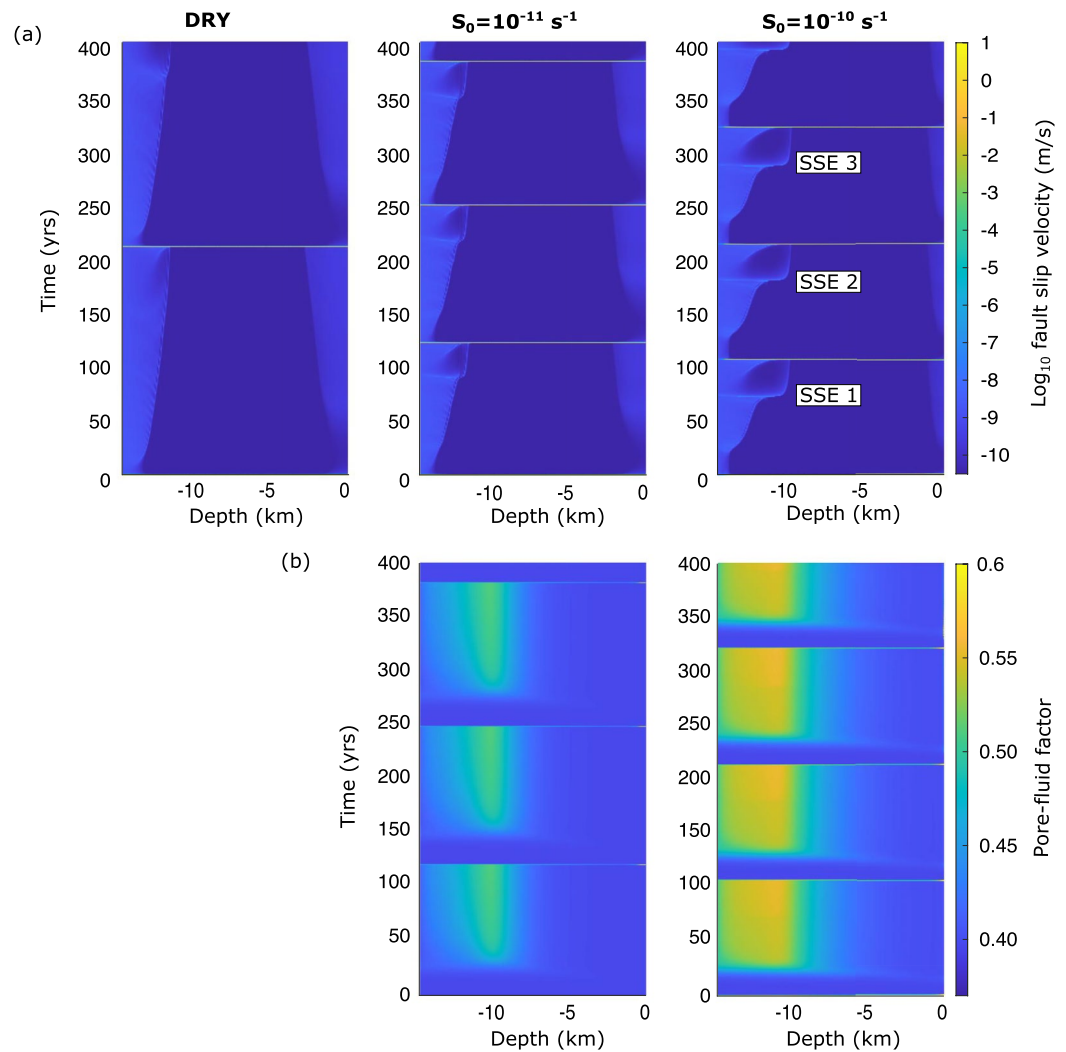


**Figure 5.** Time depth plots for a “dry” and two “wet” simulations showing the sliding velocity (a) and pore pressure ratio  $\lambda$  on the fault (b). The simulation with the highest rate of fluid production ( $S_0 = 10^{-10} \text{ s}^{-1}$ ) shows distinct slow slip events (labeled SSE 1, SSE 2 and SSE 3) in the periods between mainshocks.

#### 4. Discussion

Our modeling shows that fluids can have both a passive and active influence on earthquakes. The passive effect is due to the influence of fluid pressure in controlling the shear stress at the *onset* of rupture. We predict that if faults are highly overpressured at the time a rupture nucleates, then this will lead to significantly lower coseismic slip, stress drop, slip rates and rupture velocities and a greater tendency for pulse-like rupture propagation than if faults have lower pore pressure states. These aspects are relatively well understood and can be adequately captured by treating the fluid pressure as a tuning parameter, as was done in many previous studies (Kozdon & Dunham, 2013; Lapusta & Rice, 2003; Liu et al., 2005). However, our simulations have shown that fluids can also to play an active role in the earthquake process due to coupled spatiotemporal interactions between fluid and solid deformation, leading to phenomena such as slow slip earthquakes and delayed ruptures. Because neither of these features are observed in our models without fluid, we suggest that they are a fingerprint of fluids involvement in the earthquake process.

In our models, fluid over pressures originate from a horizontal production zone located close to the base of the seismogenic layer. This causes fluid pressures to increase over the duration of the interseismic period. During a rupture, fluid pressures on the deeper portion of the fault close to the production zone experience an abrupt

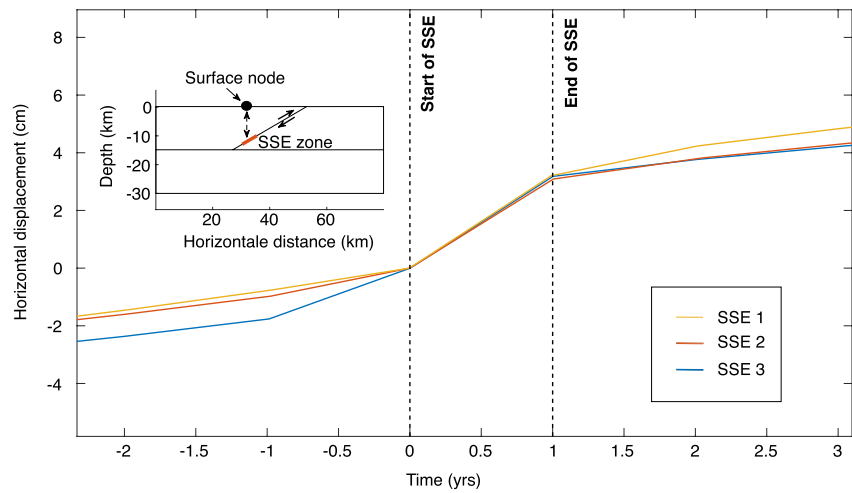


**Figure 6.** Horizontal displacement recorded at the surface directly above three slow slip events (SSEs) in a simulation with a high fluid production rate (see Figure 5, SSE 1, SSE 2, and SSE 3). The time and slip are both normalized so that they are zero at the onset of each event.

decrease: the pore fluid factor drops from about 0.5 to about 0.37, which corresponds to a pore pressure drop of about 35 MPa at 10 km depth (Figure 8, 10 km). This fluid pressure drop occurs because the high coseismic permeability enables rapid drainage up the fault. This rapid fluid redistribution means that shallower parts of the fault will typically experience an increase in fluid pressure during an earthquake (Figure 8, 8 km). Overall, we show that one can expect quite complicated variations in fluid pressure over the duration of the seismic cycle, which will depend on the local background permeability, the coseismic permeability and the location of fluid sources.

In our simulations we observe slow slip events (SSE's) that typically involve about 3 cm of slip at the surface, durations of about 1 year, and peak sliding rates of about  $10^{-7}$  m/s (see Figures 5 and 6). These characteristics are broadly consistent with longer-term SSE's in nature that are sometimes observed close to the downdip limit of the seismogenic zone on thrust faults (Frank et al., 2015; King & Chia, 2018; Obara & Kato, 2016; Wech, 2016; Yabe & Ide, 2014). These events are also markedly different from normal earthquakes, especially in terms of duration, which on the order of 1 year compared to 1 min (See Figure 7). A similar distinction has been observed for natural slip events (Ide et al., 2007). In nature, SSE's have been observed to precede larger earthquakes by a few months (Radiguet et al., 2016). Our model SSE's also precede larger fast earthquakes, though in simulations the

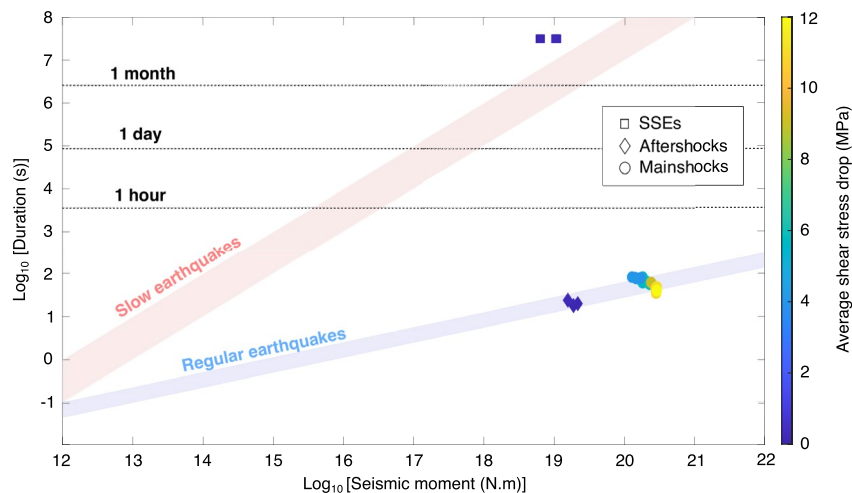


**Figure 7.** Comparison of 2D moment, average shear stress drop and duration between regular earthquakes and slow earthquakes. Also shown are the scaling relationships from Ide et al. (2007).

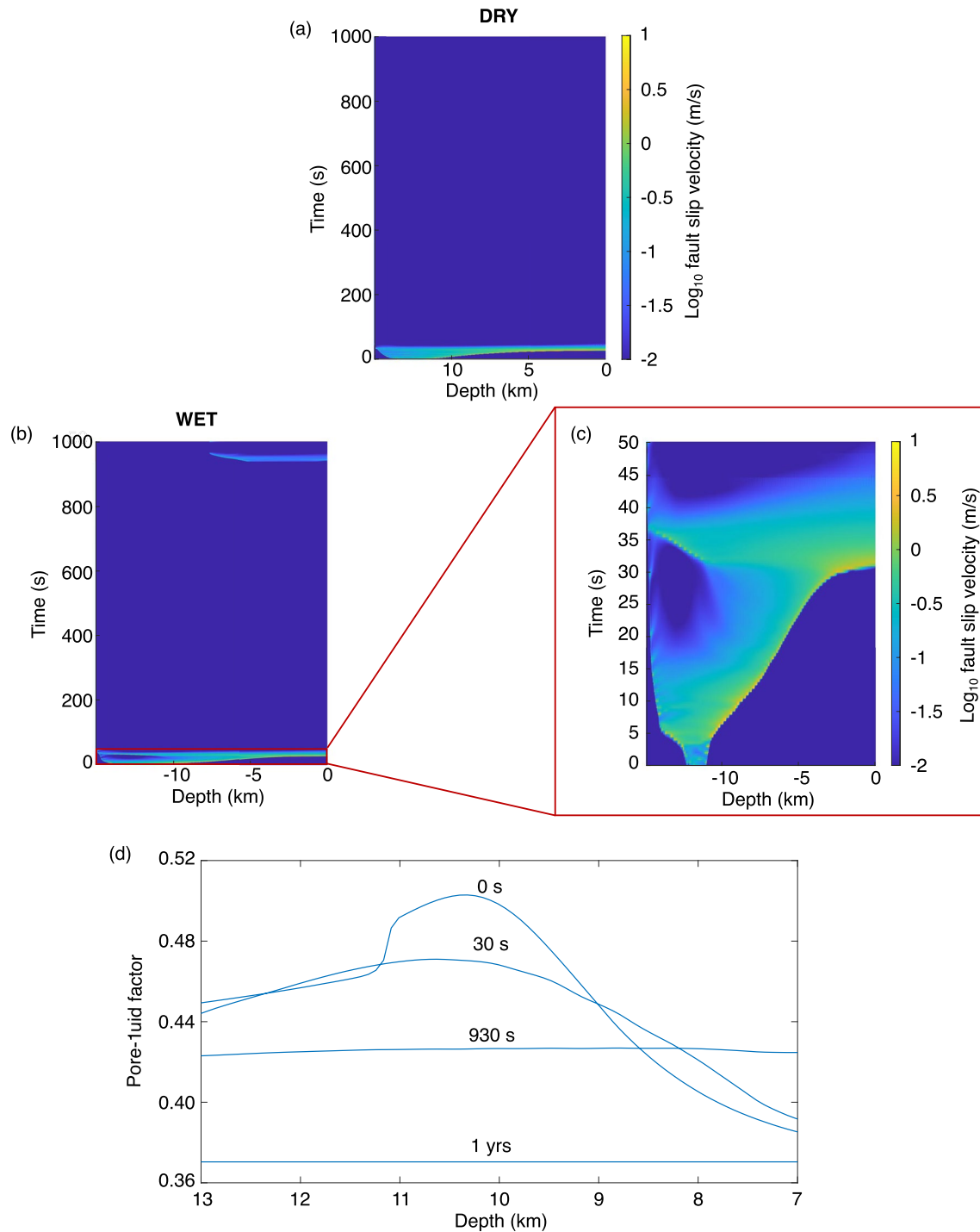


**Figure 8.** Sliding velocity along the fault during, and in the period shortly after, a large earthquake for a simulation without fluids (a) and with fluids (b), assuming  $k_{\text{max}} = 10^{-9} \text{ m}^2$  and  $S_0 = 10^{-11} \text{ s}^{-1}$ . The panel in (c) shows a zoom to illustrate detail during the main shock. (d), Pore-fluid factor on the fault at the size of maximum fluid production zone (i.e., 10 km depth), at different times after the mainshock nucleation (0, 30, 930 s, and 1 year). Note the rapid redistribution of fluid overpressures, which is linked to coseismic permeability increase.

time separation is much longer (about 30 years). The cause of SSE's in nature is unclear but fluids have long been suspected to play a critical role (Petrini et al., 2020; Warren-Smith et al., 2019). Liu and Rice (Liu & Rice, 2005) and Rubin (2008) investigated conditions for SSEs in numerical models based rate- and state-variable friction laws. In these studies, slow slip events are favored by a low effective normal stresses and/or large slip weakening

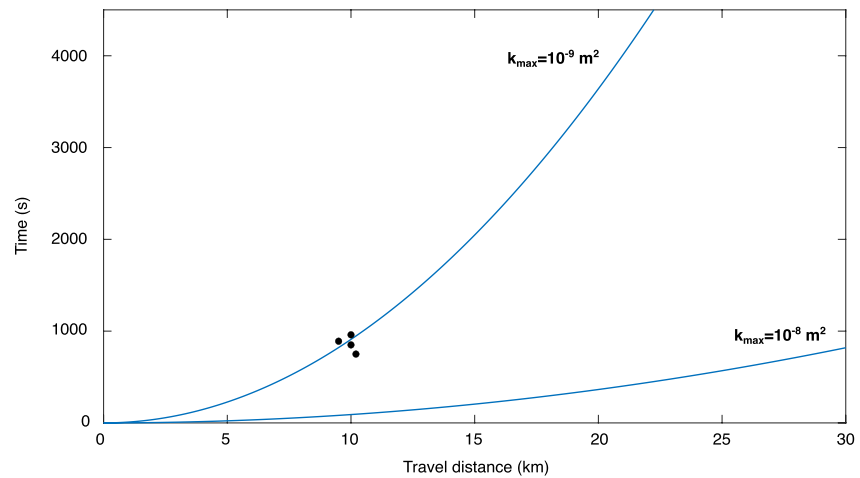


**Figure 9.** Fluid diffusion time scales versus diffusion length scales (blue curves) for two different coseismic fault permeabilities (see Equation 14). Other parameters are listed in Table 1. Black points show durations-distances between mainshocks and aftershocks in simulations with  $k_{\max} = 10^{-9} \text{ m}^2$ . We have no aftershocks when  $k_{\max} = 10^{-8} \text{ m}^2$  because fluid pressure pulse equilibrate rapidly (same order compared to the rupture time).

distances. Although our study is broadly consistent with these results, we show that SSE's can occur at surprisingly high effective stresses (i.e., when the pore pressure is only 55% of the lithostatic pressure). This difference is probably linked to the fact that we have included full poro-elastic coupling. Thus, in our model, pore pressure reduction during initial rupture propagation (induced by volumetric expansion) can act to stabilize the sliding instability, leading to SSE's. Indeed, we observed no SSE's in models where poro-elastic effects were omitted (i.e., term two on the right hand side of Equation 6, see Figure 10).

Our simulations show that fluid redistribution enabled by an abrupt increase in permeability on the fault during a large rupture (see Figure 2a) provides a mechanism for generating delayed secondary ruptures. These events are similar to aftershocks in that they always follow a main shock. However, in our models the delayed slip events occur as single ruptures rather than swarms that decay with time, as is typical of true aftershocks (Ömori, 1894; Utsu, 1961; Dieterich, 1994; Scholz, 1998). While fluid redistribution is certainly not the only possible cause of these events (Agh-Atabai & Hajati, 2014; Utkucu et al., 2016), the results here are consistent with the modeling studies of Miller et al. (2004), Miller (2020), and Zhu et al. (2020). Miller (2020) suggested that the decay in

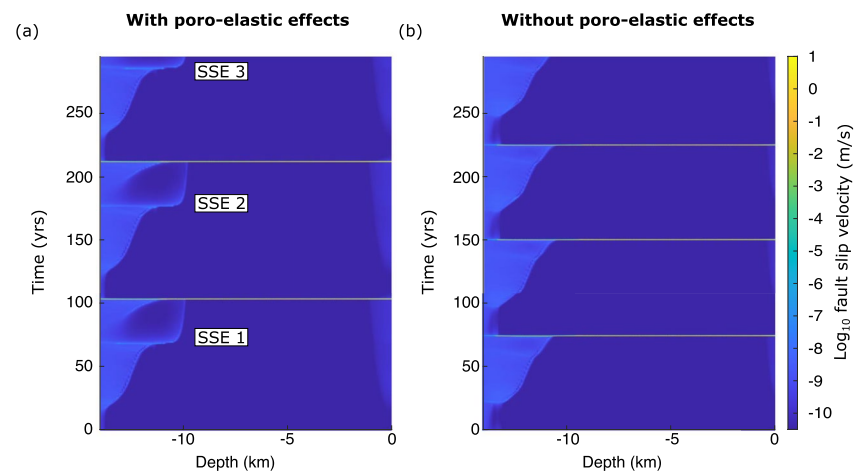


**Figure 10.** Time depth plots showing the sliding velocity for “wet” simulations ( $S_0 = 10^{-10} \text{ s}^{-1}$ ) with (a) and without (b) poro-viscoelastic effects (i.e., pore pressure variation induced by volumetric deformation of the poro-elastic solid). The simulation with the poro-viscoelastic effects shows distinct slow slip events (labeled SSE 1, SSE 2 and SSE 3) in the periods between mainshocks.

the rate of aftershocks is controlled by the rate at which a fault (permeability) reseals after a mainshock. In our study, we assumed exponential sealing with a characteristic healing time scale  $T_H$  of 2 years, which Miller (2020) showed to be broadly consistent with real earthquakes. A healing time scale of 2 years implies that the permeability on the fault recovers only about two orders of magnitude in the 10 years following a large earthquake (see Figure 2). In this case, the most important parameter controlling the rate of fluid redistribution is the maximum coseismic permeability  $k_{\max}$ . Relatively high coseismic permeabilities enable fluid pressure pulses to equilibrate so rapidly that any fluid affects might be indistinguishable from the main rupture (see Figure 9). However, lower coseismic permeabilities may lead to a significant delay between mainshock and subsequent fluid-driven slip events.

Although we find that earthquakes rupturing in the presence of fluid overpressures have quite different characteristics than ruptures in hydrostatically pressured crust, our simulations are not consistent with fluids causing long-term fault weakness. In our simulations, fluid pressures never exceed about 60% of the lithostatic stress and shear stresses at the onset of rupture exceed 80 MPa. These stress levels are expected to cause significant shear heating during fast ruptures (Noda et al., 2009). In addition, had we included extreme dynamic weakening (Di Toro et al., 2004; Goldsby & Tullis, 2011; Noda et al., 2009; Rice, 2006), much large stress drops would have occurred. Although we attempted simulations with fluid higher production rates, in order to investigate the influence of higher fluid overpressures, these produced unrealistically high uplift rates (even at the surface) due to poro-elastic volumetric expansion in the fluid source zone. This might suggest that fluid sources leading to fluid overpressures in the crust must be laterally localized, possibly limited to the fault zone itself (e.g., see Rice, 1992). Another aspect of our simulations that is somewhat unsatisfactory is that we find rupture velocities ( $V_r/C_s < 0.4$ ) that are significantly lower than found on many continental thrusts [which typically show  $V_r/C_s \approx 0.5 - 0.9$ ] (Chounet et al., 2018; Grandin et al., 2015; Huang et al., 2000; Powali et al., 2020). Once again, we suspect that the rupture velocities in our simulations would be more consistent with observations had we incorporated extreme dynamic weakening at high slip rates due to mechanisms such as thermal pressurization or “flash” heating (Di Toro et al., 2004; Goldsby & Tullis, 2011; Noda et al., 2009; Rice, 2006). We are currently extending our model to include effects such as this.

Finally, we note that in our models, the influence of fluids on the regular earthquakes is mainly linked to the effective stress and to dramatic variations in permeability. We have not explicitly considered dilatancy that could potentially provide an additional mechanism for reducing the fluid pressure during rapid sliding (Segall & Rice, 1995). Although we included pore pressure variations driven by changes in the volumetric deformation of the poroelastic solid (i.e., term two on the right-hand side of Equation 5), this effect is typically small (on the order of 1 MPa) in comparison to the effects driven by variations in permeability (which can induce fluid pressures changes of >10 MPa) during a fast earthquake.

## 5. Conclusions

We have developed a model that incorporates rate- and state-dependent sliding on a reverse fault embedded within a poro-elastic medium overlying a poro-viscoelastic substrate. Fluids are assumed to be generated in the upper seismogenic layer within a narrow horizontal band lying 10 km below the surface. The permeability is specified to decrease with increasing mean stress, increase dramatically during rapid sliding on the fault and drop exponentially over the interseismic period. The model is compressed from the side to simulate slow tectonic loading. Based on numerical simulations with this model we make the following conclusions.

1. Ruptures occurring in the presence of elevated fluid pressures are characterized by smaller coseismic slip, shear stress drop, peak sliding velocities, rupture velocities and recurrence times compared to models with hydrostatic fluid pressure.
2. In models with relatively high fluid production rates we observed slow slip earthquakes that precede larger and faster earthquakes by approximately 30 years. These slow slip events have durations of about 1 year, sliding rates of about  $10^{-7}$  m/s, and they produce about 3 cm of horizontal displacement at the surface.
3. Some of our models produce delayed slip (resembling aftershocks) that is driven by a fluid pressure pulse traveling up the fault once it ruptures. We find that the delay time between a mainshock and an aftershock scales with the maximum coseismic permeability and the distance over which fluid flow occurs.
4. The influence of fluids on earthquakes in our simulations is due mainly to the modulation of the effective stress and to variations in permeability that control the buildup and dissipation of fluid overpressures. Poro-elastic effects are of secondary importance, but are essential for the triggering of slow slip events.

5. Fluids have a noticeable effect on earthquake characteristics and can cause aftershocks and slow slip events even when fluid pressure at the onset of rupture is no more than 60% of the lithostatic stress.

### Conflict of Interest

The authors declare no conflicts of interest relevant to this study.

### Data Availability Statement

All the codes and algorithms used to generate and visualize the results discussed in this work are developed with Matlab R2020b software. The numerical results upon which this study is based with a Matlab script for plotting results are provided here: <https://zenodo.org/badge/latestdoi/586820248>.

### Acknowledgments

The Swiss National Science Foundation (Project 200021\_184626) is thanked for funding. Two reviewers are thanked for comments on the manuscript. We also thank Steve Miller for discussions concerning the role of fluids in the earthquake process. Concerning the AGU data policy, this manuscript is based on results computed from a numerical model and not on data obtained elsewhere by myself or others. Open access funding provided by Université de Genève.

### References

- Abercrombie, R. E., & Rice, J. R. (2005). Can observations of earthquake scaling constrain slip weakening? *Geophysical Journal International*, 162(2), 406–424. <https://doi.org/10.1111/j.1365-246x.2005.02579.x>
- Agh-Atabai, M., & Hajati, F. J. (2014). Coulomb stress changes and its correlation with aftershocks of recent Iranian reverse earthquakes. *Arabian Journal of Geosciences*, 8(5), 2983–2995. <https://doi.org/10.1007/s12517-014-1359-1>
- Allmann, B. P., & Shearer, P. M. (2009). Global variations of stress drop for moderate to large earthquakes. *Journal of Geophysical Research*, 114(B1). <https://doi.org/10.1029/2008jb005821>
- Andrews, D. (1976). Rupture velocity of plane strain shear cracks. *Journal of Geophysical Research*, 81(32), 5679–5687. <https://doi.org/10.1029/jb081i032p05679>
- Bizzarri, A. (2012). Rupture speed and slip velocity: What can we learn from simulated earthquakes? *Earth and Planetary Science Letters*, 317, 196–203. <https://doi.org/10.1016/j.epsl.2011.11.023>
- Brace, W., Walsh, J., & Frangos, W. (1968). Permeability of granite under high pressure. *Journal of Geophysical Research*, 73(6), 2225–2236. <https://doi.org/10.1029/jb073i006p02225>
- Chester, F., & Logan, J. M. (1986). Implications for mechanical properties of brittle faults from observations of the Punchbowl fault zone, California. *Pure and Applied Geophysics*, 124(1), 79–106. <https://doi.org/10.1007/bf00875720>
- Chounet, A., Vallée, M., Causse, M., & Courboux, F. (2018). Global catalog of earthquake rupture velocities shows anticorrelation between stress drop and rupture velocity. *Tectonophysics*, 733, 148–158. <https://doi.org/10.1016/j.tecto.2017.11.005>
- Connolly, J. (1997). Devolatilization-generated fluid pressure and deformation-propagated fluid flow during prograde regional metamorphism. *Journal of Geophysical Research*, 102(B8), 18149–18173. <https://doi.org/10.1029/97jb00731>
- Cox, S. F. (2005). *Coupling between deformation, fluid pressures, and fluid flow in ore-producing hydrothermal systems at depth in the crust*. In *One Hundredth Anniversary Volume*, Society of Economic Geologists.
- Cox, S. F., & Munroe, S. M. (2016). Breccia formation by particle fluidization in fault zones: Implications for transitory, rupture-controlled fluid flow regimes in hydrothermal systems. *American Journal of Science*, 316(3), 241–278. <https://doi.org/10.2475/03.2016.02>
- Dal Zilio, L., & Gerya, T. (2022). Subduction earthquake cycles controlled by episodic fluid pressure cycling. *Lithos*, 426, 106800. <https://doi.org/10.1016/j.lithos.2022.106800>
- Dal Zilio, L., Hegyi, B., Behr, W., & Gerya, T. (2022). Hydro-mechanical earthquake cycles in a poro-visco-elasto-plastic fluid-bearing fault structure. *Tectonophysics*, 838, 229516. <https://doi.org/10.1016/j.tecto.2022.229516>
- Day, S. M., Dalguer, L. A., Lapusta, N., & Liu, Y. (2005). Comparison of finite difference and boundary integral solutions to three-dimensional spontaneous rupture. *Journal of Geophysical Research: Solid Earth*, 110(B12), B12307. <https://doi.org/10.1029/2005jb003813>
- Di Toro, G., Goldsby, D. L., & Tullis, T. E. (2004). Friction falls towards zero in quartz rock as slip velocity approaches seismic rates. *Nature*, 427(6973), 436–439. <https://doi.org/10.1038/nature02249>
- Dieterich, J. H. (1978). Time-dependent friction and the mechanics of stick-slip. In *Rock friction and earthquake prediction* (pp. 790–806). Springer.
- Dieterich, J. H. (1979). Modeling of rock friction: 1. Experimental results and constitutive equations. *Journal of Geophysical Research: Solid Earth*, 84(B5), 2161–2168. <https://doi.org/10.1029/jb084i05p02161>
- Dieterich, J. H. (1994). A constitutive law for rate of earthquake production and its application to earthquake clustering. *Journal of Geophysical Research: Solid Earth*, 99(B2), 2601–2618. <https://doi.org/10.1029/93jb02581>
- Etheridge, M. A., Wall, V., Cox, S., & Vernon, R. (1984). High fluid pressures during regional metamorphism and deformation: Implications for mass transport and deformation mechanisms. *Journal of Geophysical Research*, 89(B6), 4344–4358. <https://doi.org/10.1029/jb089i06p04344>
- Evans, J. P., Forster, C. B., & Goddard, J. V. (1997). Permeability of fault-related rocks, and implications for hydraulic structure of fault zones. *Journal of Structural Geology*, 19(11), 1393–1404. [https://doi.org/10.1016/s0191-8141\(97\)00057-6](https://doi.org/10.1016/s0191-8141(97)00057-6)
- Fisher, D. M., Brantley, S. L., Everett, M., & Dzvovnik, J. (1995). Cyclic fluid flow through a regionally extensive fracture network within the Kodiak accretionary prism. *Journal of Geophysical Research: Solid Earth*, 100(B7), 12881–12894. <https://doi.org/10.1029/94jb02816>
- Frank, W. B., Radiguet, M., Rousset, B., Shapiro, N. M., Husker, A. L., Kostoglodov, V., et al. (2015). Uncovering the geodetic signature of silent slip through repeating earthquakes. *Geophysical Research Letters*, 42(8), 2774–2779. <https://doi.org/10.1002/2015gl063685>
- Gischig, V. S. (2015). Rupture propagation behavior and the largest possible earthquake induced by fluid injection into deep reservoirs. *Geophysical Research Letters*, 42(18), 7420–7428. <https://doi.org/10.1002/2015gl065072>
- Goldsby, D. L., & Tullis, T. E. (2011). Flash heating leads to low frictional strength of crustal rocks at earthquake slip rates. *Science*, 334(6053), 216–218. <https://doi.org/10.1126/science.1207902>
- Grandin, R., Vallée, M., Satriano, C., Lacassin, R., Klingner, Y., Simoes, M., & Bollinger, L. (2015). Rupture process of the Mw=7.9 2015 Gorkha earthquake (Nepal): Insights into Himalayan megathrust segmentation. *Geophysical Research Letters*, 42(20), 8373–8382. <https://doi.org/10.1002/2015gl066044>
- Heap, M. J., & Kennedy, B. M. (2016). Exploring the scale-dependent permeability of fractured andesite. *Earth and Planetary Science Letters*, 447, 139–150. <https://doi.org/10.1016/j.epsl.2016.05.004>

- Hedenquist, J. W., & Lowenstern, J. B. (1994). The role of magmas in the formation of hydrothermal ore deposits. *Nature*, *370*(6490), 519–527. <https://doi.org/10.1038/370519a0>
- Huang, B.-S., Chen, K.-C., Huang, W.-G., Wang, J.-H., Chang, T.-M., Hwang, R.-D., et al. (2000). Characteristics of strong ground motion across a thrust fault tip from the September 21, 1999, Chi-Chi, Taiwan earthquake. *Geophysical Research Letters*, *27*(17), 2729–2732. <https://doi.org/10.1029/2000gl011396>
- Ide, S., Beroza, G. C., Shelly, D. R., & Uchide, T. (2007). A scaling law for slow earthquakes. *Nature*, *447*(7140), 76–79. <https://doi.org/10.1038/nature05780>
- Im, K., Elsworth, D., & Wang, C. (2019). Cyclic permeability evolution during repose then reactivation of fractures and faults. *Journal of Geophysical Research: Solid Earth*, *124*(5), 4492–4506. <https://doi.org/10.1029/2019jb017309>
- Ishibashi, T., Elsworth, D., Fang, Y., Riviere, J., Madara, B., Asanuma, H., et al. (2018). Friction-stability-permeability evolution of a fracture in granite. *Water Resources Research*, *54*(12), 9901–9918. <https://doi.org/10.1029/2018wr022598>
- King, C.-Y., & Chia, Y. (2018). Anomalous streamflow and groundwater-level changes before the 1999 M7. 6 Chi–Chi earthquake in Taiwan: Possible mechanisms. *Pure and Applied Geophysics*, *175*(7), 2435–2444. <https://doi.org/10.1007/s00024-017-1737-1>
- Kozdon, J. E., & Dunham, E. M. (2013). Rupture to the trench: Dynamic rupture simulations of the 11 March 2011 Tohoku earthquake. *Bulletin of the Seismological Society of America*, *103*(2B), 1275–1289. <https://doi.org/10.1785/0120120136>
- Lamur, A., Kendrick, J., Eggertsson, G., Wall, R., Ashworth, J., & Lavallée, Y. (2017). The permeability of fractured rocks in pressurised volcanic and geothermal systems. *Scientific Reports*, *7*(1), 1–9. <https://doi.org/10.1038/s41598-017-05460-4>
- Lapusta, N., & Rice, J. R. (2003). Nucleation and early seismic propagation of small and large events in a crustal earthquake model. *Journal of Geophysical Research: Solid Earth*, *108*(B4). <https://doi.org/10.1029/2001jb000793>
- Lapusta, N., Rice, J. R., Ben-Zion, Y., & Zheng, G. (2000). Elastodynamic analysis for slow tectonic loading with spontaneous rupture episodes on faults with rate-and state-dependent friction. *Journal of Geophysical Research: Solid Earth*, *105*(B10), 23765–23789. <https://doi.org/10.1029/2000jb900250>
- Leclère, H., Faulkner, D., Llana-Fúnez, S., Bedford, J., & Wheeler, J. (2018). Reaction fronts, permeability and fluid pressure development during dehydration reactions. *Earth and Planetary Science Letters*, *496*, 227–237. <https://doi.org/10.1016/j.epsl.2018.05.005>
- Liu, S.-F., Nummedal, D., Yin, P.-G., & Luo, H.-J. (2005). Linkage of Sevier thrusting episodes and Late Cretaceous foreland basin megasequences across southern Wyoming (USA). *Basin Research*, *17*(4), 487–506. <https://doi.org/10.1111/j.1365-2117.2005.00277.x>
- Liu, Y., & Rice, J. R. (2005). Aseismic slip transients emerge spontaneously in three-dimensional rate and state modeling of subduction earthquake sequences. *Journal of Geophysical Research: Solid Earth*, *110*(B8), B08307. <https://doi.org/10.1029/2004jb003424>
- Manning, C., & Ingebritsen, S. (1999). Permeability of the continental crust: Implications of geothermal data and metamorphic systems. *Reviews of Geophysics*, *37*(1), 127–150. <https://doi.org/10.1029/1998rg900002>
- Marone, C. (1998). The effect of loading rate on static friction and the rate of fault healing during the earthquake cycle. *Nature*, *391*(6662), 69–72. <https://doi.org/10.1038/34157>
- McClure, M. W. (2015). Generation of large postinjection-induced seismic events by backflow from dead-end faults and fractures. *Geophysical Research Letters*, *42*(16), 6647–6654. <https://doi.org/10.1002/2015gl065028>
- McClure, M. W., & Horne, R. N. (2011). Investigation of injection-induced seismicity using a coupled fluid flow and rate/state friction model. *Geophysics*, *76*(6), WC181–WC198. <https://doi.org/10.1190/geo2011-0064.1>
- Miller, S. A. (1997). *The behavior of 3-dimensional fluid-controlled earthquake model: Applications and implications (unpublished doctoral dissertation)*. ETH Zurich.
- Miller, S. A. (2020). Aftershocks are fluid-driven and decay rates controlled by permeability dynamics. *Nature Communications*, *11*(1), 1–11. <https://doi.org/10.1038/s41467-020-19590-3>
- Miller, S. A., Collettini, C., Chiaraluce, L., Cocco, M., Barchi, M., & Kaus, B. J. (2004). Aftershocks driven by a high-pressure CO<sub>2</sub> source at depth. *Nature*, *427*(6976), 724–727. <https://doi.org/10.1038/nature02251>
- Miller, S. A., & Nur, A. (2000). Permeability as a toggle switch in fluid-controlled crustal processes. *Earth and Planetary Science Letters*, *183*(1–2), 133–146. [https://doi.org/10.1016/S0012-821X\(00\)00263-6](https://doi.org/10.1016/S0012-821X(00)00263-6)
- Noda, H., Dunham, E. M., & Rice, J. R. (2009). Earthquake ruptures with thermal weakening and the operation of major faults at low overall stress levels. *Journal of Geophysical Research*, *114*(B7), B07302. <https://doi.org/10.1029/2008jb006143>
- Noda, H., Lapusta, N., & Rice, J. R. (2011). Earthquake sequence calculations with dynamic weakening mechanisms. In *Multiscale and multiphysics processes in geomechanics* (pp. 149–152). Springer.
- Noir, J., Jacques, E., Bekri, S., Adler, P., Tapponnier, P., & King, G. (1997). Fluid flow triggered migration of events in the 1989 Dobi earthquake sequence of central Afar. *Geophysical Research Letters*, *24*(18), 2335–2338. <https://doi.org/10.1029/97gl02182>
- Obara, K., & Kato, A. (2016). Connecting slow earthquakes to huge earthquakes. *Science*, *353*(6296), 253–257. <https://doi.org/10.1126/science.aaf1512>
- Oglesby, D. D., Archuleta, R. J., & Nielsen, S. B. (1998). Earthquakes on dipping faults: The effects of broken symmetry. *Science*, *280*(5366), 1055–1059. <https://doi.org/10.1126/science.280.5366.1055>
- Osborne, M. J., & Swarbrick, R. E. (1998). Mechanisms for generating overpressure in sedimentary basins: A reevaluation. *AAPG Bulletin*, *82*(12), 2270–2271.
- Omori, F. (1894). *On the aftershocks of earthquakes* (Vol. 7, pp. 111–120). Journal of the College of Science. Imperial University of Tokyo.
- Palmer, A. C., & Rice, J. R. (1973). The growth of slip surfaces in the progressive failure of over-consolidated clay. *Proceedings of the Royal Society of London. A. Mathematical and Physical Sciences*, *332*(1591), 527–548.
- Passelègue, F. X., Almakari, M., Dublanche, P., Barras, F., Fortin, J., & Violay, M. (2020). Initial effective stress controls the nature of earthquakes. *Nature Communications*, *11*(1), 1–8. <https://doi.org/10.1038/s41467-020-18937-0>
- Passelègue, F. X., Schubnel, A., Nielsen, S., Bhat, H. S., Deldicque, D., & Madariaga, R. (2016). Dynamic rupture processes inferred from laboratory microearthquakes. *Journal of Geophysical Research: Solid Earth*, *121*(6), 4343–4365. <https://doi.org/10.1002/2015jb012694>
- Petrini, C., Gerya, T., Yarushina, V., van Dinther, Y., Connolly, J., & Madonna, C. (2020). Seismo-hydro-mechanical modelling of the seismic cycle: Methodology and implications for subduction zone seismicity. *Tectonophysics*, *791*, 228504. <https://doi.org/10.1016/j.tecto.2020.228504>
- Powali, D., Sharma, S., Mandal, R., & Mitra, S. (2020). A reappraisal of the 2005 Kashmir (Mw 7.6) earthquake and its aftershocks: Seismotectonics of NW Himalaya. *Tectonophysics*, *789*, 228501. <https://doi.org/10.1016/j.tecto.2020.228501>
- Radiguet, M., Perfettini, H., Cotte, N., Gualandi, A., Valette, B., Kostoglodov, V., et al. (2016). Triggering of the 2014 Mw7. 3 Papanoa earthquake by a slow slip event in Guerrero, Mexico. *Nature Geoscience*, *9*(11), 829–833. <https://doi.org/10.1038/ngeo2817>
- Renard, F., Gratier, J.-P., & Jamveit, B. (2000). Kinetics of crack-sealing, intergranular pressure solution, and compaction around active faults. *Journal of Structural Geology*, *22*(10), 1395–1407. [https://doi.org/10.1016/S0191-8141\(00\)00064-x](https://doi.org/10.1016/S0191-8141(00)00064-x)

- Rice, J. R. (1992). Fault stress states, pore pressure distributions, and the weakness of the San Andreas fault. *International Geophysics*, 51, 475–503.
- Rice, J. R. (2006). Heating and weakening of faults during earthquake slip. *Journal of Geophysical Research: Solid Earth*, 111(B5). <https://doi.org/10.1029/2005jb004006>
- Rubin, A. M. (2008). Episodic slow slip events and rate-and-state friction. *Journal of Geophysical Research: Solid Earth*, 113(B11), B11414. <https://doi.org/10.1029/2008jb005642>
- Ruina, A. (1983). Slip instability and state variable friction laws. *Journal of Geophysical Research: Solid Earth*, 88(B12), 10359–10370. <https://doi.org/10.1029/jb088ib12p10359>
- Scala, A., Festa, G., Vilotte, J.-P., Lorito, S., & Romano, F. (2019). Wave interaction of reverse-fault rupture with free surface: Numerical analysis of the dynamic effects and fault opening induced by symmetry breaking. *Journal of Geophysical Research: Solid Earth*, 124(2), 1743–1758. <https://doi.org/10.1029/2018jb016512>
- Scholz, C. H. (1998). Earthquakes and friction laws. *Nature*, 391(6662), 37–42. <https://doi.org/10.1038/34097>
- Scholz, C. H. (2006). Strength of faults and maximum stress drops in earthquakes. In Report of the Workshop on Extreme Ground Motions at Yucca Mountain, August 23–25, 2004. Open-File Rept. 2006-1277. US Geological Survey, Reston, Virginia.
- Segall, P., & Rice, J. R. (1995). Dilatancy, compaction, and slip instability of a fluid-infiltrated fault. *Journal of Geophysical Research: Solid Earth*, 100(B11), 22155–22171. <https://doi.org/10.1029/95jb02403>
- Selvadurai, A., Boulon, M., & Nguyen, T. (2005). The permeability of an intact granite. *Pure and Applied Geophysics*, 162(2), 373–407. <https://doi.org/10.1007/s00024-004-2606-2>
- Sibson, R. H. (1986). Rupture interaction with fault jogs. *Earthquake Source Mechanics*, 37, 157–167.
- Sibson, R. H. (1990). Conditions for fault-valve behaviour. *Geological Society, London, Special Publications*, 54(1), 15–28. <https://doi.org/10.1144/gsl.sp.1990.054.01.02>
- Sibson, R. H. (1992). Implications of fault-valve behaviour for rupture nucleation and recurrence. *Tectonophysics*, 211(1–4), 283–293. [https://doi.org/10.1016/0040-1951\(92\)90065-e](https://doi.org/10.1016/0040-1951(92)90065-e)
- Sibson, R. H. (2017). Tensile overpressure compartments on low-angle thrust faults. *Earth Planets and Space*, 69(1), 1–15. <https://doi.org/10.1186/s40623-017-0699-y>
- Sibson, R. H., Robert, F., & Poulsen, K. H. (1988). High-angle reverse faults, fluid-pressure cycling, and mesothermal gold-quartz deposits. *Geology*, 16(6), 551–555. [https://doi.org/10.1130/0091-7613\(1988\)016<0551:harffp>2.3.co;2](https://doi.org/10.1130/0091-7613(1988)016<0551:harffp>2.3.co;2)
- Simpson, G. (2017). *Practical finite element modeling in earth science using Matlab*. John Wiley & Sons.
- Simpson, G. (2018). What do earthquakes reveal about ambient shear stresses in the upper crust? *Geology*, 46(8), 703–706. <https://doi.org/10.1130/g45052.1>
- Sleep, N. H., & Blanpied, M. L. (1992). Creep, compaction and the weak rheology of major faults. *Nature*, 359(6397), 687–692. <https://doi.org/10.1038/359687a0>
- Suppe, J. (2014). Fluid overpressures and strength of the sedimentary upper crust. *Journal of Structural Geology*, 69, 481–492. <https://doi.org/10.1016/j.jsg.2014.07.009>
- Tenthorey, E., Cox, S. F., & Todd, H. F. (2003). Evolution of strength recovery and permeability during fluid–rock reaction in experimental fault zones. *Earth and Planetary Science Letters*, 206(1–2), 161–172. [https://doi.org/10.1016/s0012-821x\(02\)01082-8](https://doi.org/10.1016/s0012-821x(02)01082-8)
- Tsutsumi, A., & Shimamoto, T. (1997). High-velocity frictional properties of gabbro. *Geophysical Research Letters*, 24(6), 699–702. <https://doi.org/10.1029/97gl00503>
- Utkucu, M., Durmuş, H., & Nalbant, S. S. (2016). Stress history controls the spatial pattern of aftershocks: Case studies from strike-slip earthquakes. *International Journal of Earth Sciences*, 106(6), 1841–1861. <https://doi.org/10.1007/s00531-016-1389-x>
- Utsu, T. (1961). A statistical study on the occurrence of aftershocks. *Geophysical Magazine*, 30, 521–605.
- Walder, J., & Nur, A. (1984). Porosity reduction and crustal pore pressure development. *Journal of Geophysical Research: Solid Earth*, 89(B13), 11539–11548. <https://doi.org/10.1029/jb089ib13p11539>
- Warren-Smith, E., Fry, B., Wallace, L., Chon, E., Henrys, S., Sheehan, A., et al. (2019). Episodic stress and fluid pressure cycling in subducting oceanic crust during slow slip. *Nature Geoscience*, 12(6), 475–481. <https://doi.org/10.1038/s41561-019-0367-x>
- Wech, A. G. (2016). Extending Alaska's plate boundary: Tectonic tremor generated by Yakutat subduction. *Geology*, 44(7), 587–590. <https://doi.org/10.1130/g37817.1>
- Weis, P., Driesner, T., & Heinrich, C. A. (2012). Porphyry-copper ore shells form at stable pressure-temperature fronts within dynamic fluid plumes. *Science*, 338(6114), 1613–1616. <https://doi.org/10.1126/science.1225009>
- Xue, L., Li, H.-B., Brodsky, E. E., Xu, Z.-Q., Kano, Y., Wang, H., et al. (2013). Continuous permeability measurements record healing inside the Wenchuan earthquake fault zone. *Science*, 340(6140), 1555–1559. <https://doi.org/10.1126/science.1237237>
- Yabe, S., & Ide, S. (2014). Spatial distribution of seismic energy rate of tectonic tremors in subduction zones. *Journal of Geophysical Research: Solid Earth*, 119(11), 8171–8185. <https://doi.org/10.1002/2014jb011383>
- Zheng, G., & Rice, J. R. (1998). Conditions under which velocity-weakening friction allows a self-healing versus a cracklike mode of rupture. *Bulletin of the Seismological Society of America*, 88(6), 1466–1483.
- Zhu, W., Allison, K. L., Dunham, E. M., & Yang, Y. (2020). Fault valving and pore pressure evolution in simulations of earthquake sequences and aseismic slip. *Nature Communications*, 11(1), 1–11. <https://doi.org/10.1038/s41467-020-18598-z>